Hemodynamic timing in resting-state and breathing-task BOLD fMRI

Jingxuan Gong[1*], Rachael C. Stickland[2*], Molly G. Bright[1,2]

[1] Department of Biomedical Engineering, McCormick School of Engineering and Applied Sciences, Northwestern University, Evanston, IL, USA

[2] Department of Physical Therapy and Human Movement Sciences, Feinberg School of Medicine, Northwestern University, Chicago, IL, USA

*J.G. and R.C.S. contributed equally to this work.

Corresponding Author:

Dr. Molly Bright

645 N. Michigan Ave, Suite 1100

Chicago, IL 60611

USA

t: 1 (312) 503-5870

e: molly.bright@northwestern.edu

brightlab.northwestern.edu

Keywords: BOLD fMRI, hemodynamics, resting-state, breath-hold, relative timing

Abstract

The blood flow response to a vasoactive stimulus demonstrates regional heterogeneity across both the healthy brain and in cerebrovascular pathology. The timing of a regional hemodynamic response is emerging as an important biomarker of cerebrovascular dysfunction, as well as a methodological confound within fMRI analyses. Previous research demonstrated that hemodynamic timing is more robustly characterized when a larger systemic vascular response is evoked by a breathing challenge, compared to when only spontaneous fluctuations in vascular physiology are present (i.e., in resting-state data). However, it is not clear whether hemodynamic delays in these two conditions are physiologically interchangeable, and how methodological signal-to-noise factors may limit their agreement. To address this, we generated whole-brain maps of hemodynamic delays in nine healthy adults. We assessed the agreement of voxelwise gray matter (GM) hemodynamic delays between two conditions: resting-state and breath-holding. We found that delay values demonstrated poor agreement when considering all GM voxels, but increasingly greater agreement when limiting analyses to voxels showing strong correlation with the GM mean time-series. Voxels showing the strongest agreement with the GM mean time-series were primarily located near large venous vessels, however these voxels explain some, but not all, of the observed agreement in timing. Increasing the degree of spatial smoothing of the fMRI data enhanced the correlation between individual voxel time-series and the GM mean time-series and did not substantially change the agreement in hemodynamic timing as a function of this relationship strength. These results suggest that signal-to-noise factors may be limiting the accuracy of voxelwise timing estimates and hence their agreement between the two data segments. In conclusion, caution must be taken when using voxelwise delay estimates from resting-state and breathing-task data interchangeably, and additional work is needed to evaluate their relative sensitivity and specificity to aspects of vascular physiology and pathology.

1. Introduction

Oxygenated blood takes time to arrive at the brain, traveling from the heart and through the vascular tree to ultimately perfuse into local brain tissue where nutrient exchange can occur. Changes in blood flow can lead to changes in blood oxygenation, particularly in the venous vessels downstream of the exchange with tissue. Functional Magnetic Resonance Imaging (fMRI) is sensitive to blood flow changes due to their impact on blood oxygenation levels, referred to as Blood Oxygenation Level Dependent (BOLD) contrast (Glover, 2011). However, signals to initiate local blood flow changes will not produce instantaneous changes in BOLD fMRI signals. A single neural event evokes a local hemodynamic response through neurovascular coupling mechanisms (Huneau, Benali, & Chabriat, 2015), and this response is typically modeled with the canonical hemodynamic response function or HRF (Friston et al., 1998; Martindale et al., 2003; Penny, Friston, Ashburner, Kiebel, & Nichols, 2006). Determined empirically, this HRF peaks many seconds after an impulse of neural stimulation suggesting that there is an inherent delay in the local blood flow response to nearby neural activity. There is evidence that the shape and timing of the HRF to a neural event may vary across brain regions (Handwerker, Ollinger, & D'Esposito, 2004), with healthy aging (Issard & Gervain, 2018; West et al., 2019), and under different baseline states (Cohen, Ugurbil, & Kim, 2002; Liu et al., 2004). Blood flow changes can also be evoked by a non-neural vasodilatory stimulus such as carbon dioxide, a phenomenon known as cerebrovascular reactivity (CVR) (Chen & Gauthier, 2021; Liu, De Vis, & Lu, 2019; Pinto, Bright, Bulte, & Figueiredo, 2020; Sleight, Stringer, Marshall, Wardlaw, & Thrippleton, 2021). These responses are also delayed, with regional heterogeneity observed across the healthy brain and altered by disease (Bright, Bulte, Jezzard, & Duyn, 2009; Donahue et al., 2016; Holmes et al., 2020; Leung, Duffin, Fisher, & Kassner, 2016; Moia et al., 2020; Siegel, Snyder, Ramsey, Shulman, & Corbetta, 2016; Sousa, Vilela, & Figueiredo, 2014).

Hemodynamic delays have been estimated in resting-state BOLD fMRI data and then used to correct functional connectivity (FC) analyses, both in studies with healthy populations (Erdogan, Tong, Hocke, Lindsey, & Frederick, 2016) and when comparing FC differences between healthy populations and populations with a vascular pathology (Chi et al., 2018; Siegel et al., 2016). These corrections aim to remove a vascular confound from the data, to make the interpretation of neuronal FC more valid. There is also a growing body of literature demonstrating hemodynamic delays are more than just a confound to correct for and may be a useful clinical metric in pathologies such as moyamoya disease (Donahue et al., 2016), carotid stenosis (Chang et al., 2013), stroke (Ni et al., 2017; Siegel et al., 2016), glioma (Cai et al., 2022), and Alzheimer's (Holmes et al., 2020). However, variability in the timing of the BOLD signal will reflect several different physiological effects, and these will depend on the origin of the blood flow changes. For example, carbon dioxide changes take place in the bloodstream, and this vasodilatory signal travels with the bloodstream from the lungs to the heart, to the brain, and ultimately influences the local arteriolar vessels. Local neural activity may influence local arterioles more immediately, as their signal is transmitted through faster neurochemical pathways. Depending on a multitude of factors (design of the fMRI study, approach to

modeling the data, participant individual differences) the dominance of neural and vascular contributions to the estimated hemodynamic delays will vary, a topic which is explored further in the next paragraphs.

We define these relative hemodynamic delays (also referred to as hemodynamic 'timings', or 'lags' in the BOLD signal) as the time a BOLD amplitude change occurs with respect to an amplitude change in a reference signal (also called a 'probe regressor'). This probe regressor may be a physiological signal recorded external to the brain, typically related to cardiac or respiratory-related phenomena, as these fluctuations reflect systemic physiological effects of non-neuronal origin that drive global blood flow changes. Alternatively, a data-driven probe regressor can be used, typically the average BOLD signal in brain or grey matter tissue filtered to a certain frequency band, which is thought to mostly reflect these global systemic drivers (Liu, Li, et al., 2017; Tong, Hocke, & Frederick, 2019). In addition to the choice of probe regressor, hemodynamic delays can be mapped with a variety of stimulus designs. Firstly, a vasodilatory stimulus can be used to enhance the effect size of the corresponding non-neural BOLD signal changes. Researchers use complex gas inhalation challenges (Liu et al., 2019) as well as simple breathing tasks (e.g., breath-holding) in order to modulate blood CO_2 levels and evoke a large systemic vascular response. Breathing-tasks have been used successfully to map the variability of BOLD hemodynamic timings in both healthy and patient populations (Bright et al., 2009; Chang, Thomason, & Glover, 2008; Geranmayeh, Wise, Leech, & Murphy, 2015; Magon et al., 2009; Moia et al., 2021; Pinto, Jorge, Sousa, Vilela, & Figueiredo, 2016; Raut, Nair, Sattin, & Prabhakaran, 2016; Sousa et al., 2014). We have previously demonstrated that the timing of the BOLD CVR response is more robustly characterized when a large systemic vascular response is evoked by a breathing challenge, compared to when only spontaneous fluctuations in vascular physiology are present (Bright & Murphy, 2017; Stickland et al., 2021). Still, researchers have had success with mapping BOLD hemodynamic timings in healthy and patient populations using resting-state fMRI data in the absence of evoked responses (Cai et al., 2022; Hu et al., 2021; Liu, Li, et al., 2017; Siegel et al., 2016; Tong et al., 2019). Despite the anticipated lower signal-to-noise ratio of the vascular effects, this resting-state experimental design is simpler and therefore suitable for a wider range of populations and clinical or research contexts.

The fMRI signals recorded with the two designs mentioned, breathing-task and resting-state, contain both neural and vascular information. Thus, there is ambiguity regarding the physiological origin and specificity of the fMRI timing estimates. Although it is reasonable to assume that the majority of information present in the fMRI time-series during a breath-holding task reflects the associated evoked vascular response, there will be some neural activity associated with the voluntary performance of the task, in addition to a baseline level of intrinsic neuronal fluctuations. Similarly, fluctuating signals in resting-state fMRI data are frequently used to characterize neural activation patterns of intrinsic brain networks, but it is well established that many physiologic phenomena, both neural and vascular, influence blood flow and BOLD fMRI signals in uncontrolled ways (Caballero-Gaudes & Reynolds, 2017; Liu, 2013, 2016; Murphy, Birn, & Bandettini, 2013; Tong et al., 2019). Thus, these two types of

fMRI data – breathing-task and resting-state – contain both neural and vascular information, albeit with different weightings.

To mitigate the confounding influence of vascular physiology on traditional fMRI activation and FC results, researchers have implemented scaling or regression techniques using CVR-related BOLD amplitudes (Handwerker, Gazzaley, Inglis, & D'Esposito, 2007; Kannurpatti & Biswal, 2008; Murphy, Harris, & Wise, 2011; Thomason, Foland, & Glover, 2007; Tsvetanov et al., 2015). As well as influencing activation amplitudes, variability in BOLD hemodynamic timings may also mask true neural effects and introduce spurious noise into output metrics if not accounted for properly. For example, a temporal offset in the vascular response of two brain regions with synchronous neural activity could mask their relationship in a standard correlative resting-state fMRI analysis, or improperly suggest an anti-correlative relationship. Therefore, researchers have incorporated cross-correlation and coherence-based measures in resting-state FC analyses, rather than simple correlations, to be less confounded by the relative phase of the BOLD signal (Erdogan et al., 2016; Murphy et al., 2011). These timing corrections may be especially important for patient populations with larger arterial arrival delays in some regions (Jahanian, Christen, Moseley, & Zaharchuk, 2018). However, the best way to estimate, and therefore correct for, hemodynamic timings is not always clear, as resting-state fMRI data includes low-frequency signal contributions from many physiological sources. There is less consensus when analyzing BOLD timing, compared to BOLD amplitude, regarding how this information can be interpreted and applied. The more specific and robust measures of hemodynamic timings estimated with breath-hold data have been used to correct timings in task and resting-state fMRI data, with the aim of removing hemodynamic biases from task-based and FC analyses (Chang et al., 2008; Li et al., 2018). However, corrections such as these are currently done without strong evidence that hemodynamic timings in these two conditions are theoretically interchangeable. In order to understand what these relative hemodynamic timing estimates represent, and how we can use them in future fMRI analyses, it is critical we examine the relationship between hemodynamic timings measured using different types of input data.

In this paper, we estimate hemodynamic timings (delays) across the brain in BOLD fMRI data from healthy participants. We assess the agreement of hemodynamic timing estimates derived from data that contained a breath-hold task and from data that only contained resting-state (spontaneous) fluctuations, to understand how similar these timing estimates are in an individual. To further interpret our assessment of the agreement, we applied amplitude thresholds (Chang et al., 2008; Fesharaki et al., 2021) and different levels of smoothing of the input data, hypothesizing that signal-to-noise factors would modulate the absolute agreement of hemodynamic timing estimates. We also investigated which areas of the brain (if any) had the highest agreement, to help provide anatomical insight into what may be driving agreement or disagreement. Comparing these two paradigms may shed light on their different physiological drivers, or suggest they provide similar information under certain

methodological constraints, which is useful for researchers to know when choosing a paradigm to assess or correct for hemodynamic timings in BOLD fMRI studies.

2. Methods

The data from this study unfortunately cannot be made openly available due to restrictions of the ethical approval that they were collected under. However, within ethical restrictions, analytic derivatives not included in this publication may be supplied upon request. The visual instructions for the breathing tasks, displayed during scanning, were created with PsychoPy code (Stickland, Bright, Moia, & Zvolanek, 2022) and the hemodynamic timing estimates were produced with the *Rapidtide* Toolbox v2.0.9 (Frederick, 2016-2022). Specific details on how these coding repositories were used, as well as other primary analysis code for this project, have been organized into this GitHub repository: github.com/BrightLab-ANVIL/Gong_2022.

2.1 Data acquisition

This study was reviewed by Northwestern University's Institutional Review Board. Written informed consent was obtained from all subjects. Nine healthy volunteers were included in the study (6 females, mean age = 26.2±4.1 years).

A 3T Siemens Prisma MRI system with a 64-channel head coil was used to collect neuroimaging data. The functional T2*-weighted acquisitions run during the hybrid breathing-task and resting-state protocol (Figure 1A) were gradient-echo planar sequences provided by the Center for Magnetic Resonance Research (CMRR, Minnesota) with the following parameters: TR/TE = 1200/34.4 ms, FA = 62°, Multi-Band (MB) acceleration factor = 4, 60 axial slices with an ascending interleaved order, 2 mm isotropic voxels, FOV = 208 × 208 mm^2, Phase Encoding = AP, phase partial Fourier = 7/8, Bandwidth = 2290 Hz/Px. One single-band reference (SBRef) volume was acquired before the functional T2*-weighted acquisition (the same scan acquisition parameters without the MB acceleration factor) to facilitate functional realignment and masking. A whole brain T1-weighted EPI-navigated multi-echo MPRAGE scan was acquired, adapted from (Tisdall et al., 2016), with these parameters: 1 mm isotropic resolution, 176 sagittal slices, TR/TE1/TE2/TE3 = 2170/1.69/3.55/5.41 ms, TI = 1160 ms, FA = 7°, FOV = 256 × 256, Bandwidth = 650 Hz, acquisition time of 5 minutes 12 seconds, including 24 reacquisition TRs. The three echo images were combined using root-mean-square.

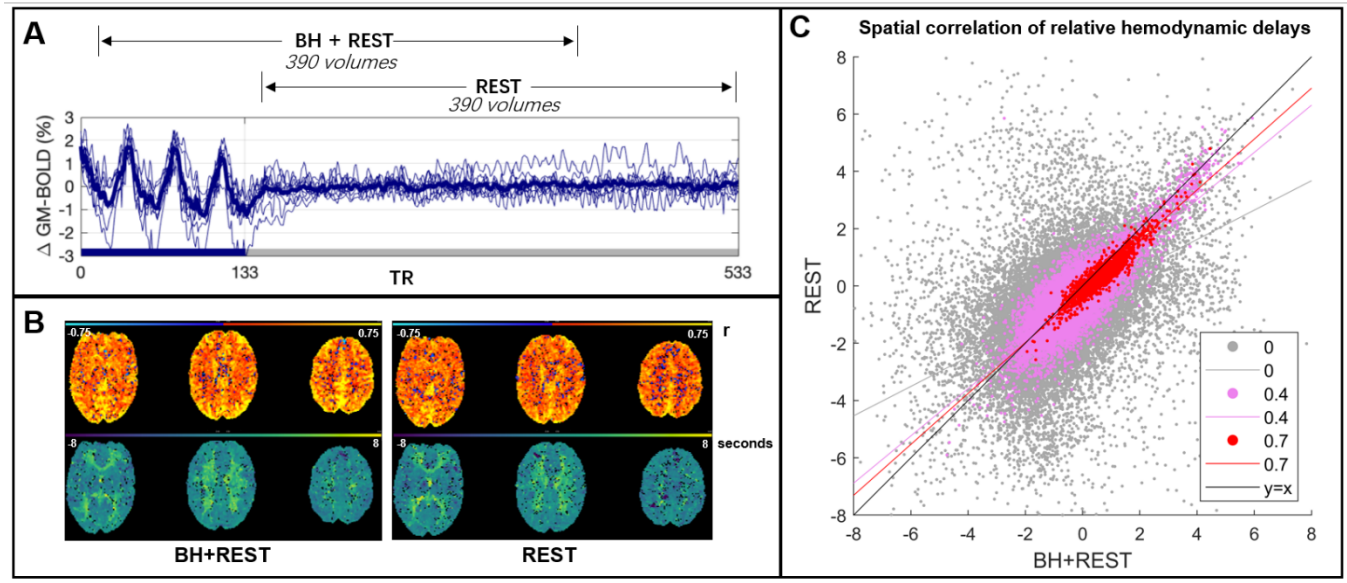

Figure 1. *Panel A: The BOLD time-series averaged across gray matter (GM) for each subject (thinner blue lines) and the group average (thicker line). This time-series data was cut into two segments: one segment, BH+REST, includes a breathing task (solid blue bar on x-axis) followed by REST and the second segment is only REST. 390 volumes amount to 7 mins 48 s (TR=1.2 s). Panel B: The output maps, from Rapidtide, for one example subject. The top row shows the correlation amplitude at each voxel (maximum correlation coefficient between each voxel time-series and probe regressor). The bottom row shows the relative delays at each voxel (time in seconds when the maximum correlation occurred). Panel C: Spatial correlation, in GM voxels, between hemodynamic delay times (panel B, bottom) from the BH+REST and REST data segments of an example subject. The correlation amplitude (panel B, top) is used to threshold the delays; the figure legend shows 3 examples of amplitude thresholding we applied. Each dot represents a voxel passing the threshold for both data segments, e.g., 0 = hemodynamic delay for a specific voxel must be in GM and have a correlation amplitude greater than 0 to be included. The lines are linear regression lines. For comparison, the y=x line is also shown.*

Previous work with similar tasks (Bright et al., 2009; Lipp, Murphy, Caseras, & Wise, 2015) was used as guidance for the breath-hold (BH) task timings. Subjects practiced the BH tasks outside the scanner with the researcher (R.C.S) prior to scanning. During the scan, subjects performed three BH cycles (paced breathing and a 15-second end-expiration hold) followed by an 8-minute period of rest with visual fixation. Two equal-length data segments (Figure 1A) were analyzed: one comprised the breathing task followed by rest (BH+REST), whereas the other just included rest (REST). These neuroimaging data were used within previously published work (Stickland et al., 2021).

2.2 Data analysis

2.2.1 Data preprocessing

A custom shell script grouped AFNI (Cox, 1996) and FSL (Jenkinson, Beckmann, Behrens, Woolrich, & Smith, 2012; Li, Morgan, Ashburner, Smith, & Rorden, 2016; Smith et al., 2004; Woolrich et al., 2009) commands. DICOMS were converted to NIFTI format with dcm2niiX (Li et al., 2016). For motion correction of the fMRI dataset, AFNI's 3dvolreg was performed with the SBRef as the reference volume; six motion parameters (three translations, three rotations) were extracted, demeaned, and saved. The first 10 volumes were discarded to allow the signal to achieve a steady state of magnetization and then brain extraction (Smith, 2002) was performed using FSL. The T1-weighted dataset was processed with the fsl_anat function, involving brain extraction, bias field correction, and tissue segmentation with FAST (Zhang, Brady, & Smith, 2001). A GM tissue mask was subsequently created by thresholding the partial volume estimate image to 0.5 and transforming it to the subject-specific fMRI space with FSL's FLIRT command (Jenkinson, Bannister, Brady, & Smith, 2002; Jenkinson & Smith, 2001). The fMRI dataset was portioned into two segments (BH+REST and REST), each containing 390 volumes (Figure 1A). Finally, detrending and denoising were performed via linear regression using AFNI's 3dTproject command, including the removal of Legendre polynomials up to the 4th degree to remove drifts in the signal and the six motion parameters. This single-subject preprocessed fMRI dataset, divided into two equal-length segments, was the input to the *Rapidtide* function, explained below.

The MNI structural atlas (Collins, Holmes, Peters, & Evans, 1995; Kötter et al., 2001), which parcellates the brain into 9 anatomical regions (caudate, cerebellum, frontal lobe, insula, occipital lobe, parietal lobe, putamen, temporal lobe, thalamus), was linearly transformed to fMRI subject space using FSL FLIRT, then masked to the subject's GM. This transformation was achieved using nearest neighbor interpolation and 12 degrees of freedom and concatenating previously created registration matrices (the functional to structural space registration matrix and the structural to MNI registration matrix were previously created from running the fsl_anat function).

2.2.2 Estimation of relative hemodynamic timings

The *Rapidtide* toolbox (v2.0.9), previously called *Riptide,* was used to perform time-lagged correlations between the preprocessed fMRI voxel time-series and a data-driven probe regressor (initially defined as the mean GM time-series). *Rapidtide* is a suite of python programs that performs rapid time delay analysis in filtered fMRI data to find lagged correlations between each voxel's time-series and a reference time-series, referred to as a "probe regressor" (Frederick, 2016-2022). We chose to use the *Rapidtide* toolbox to estimate these relative hemodynamic timings because: (i) it is a citable open-source software package, (ii) it has been demonstrated to be successful when applied

to resting-state data (Champagne et al., 2022; Erdogan et al., 2016) and (iii) with a data-driven probe regressor, the resting-state and breath-hold data can be analyzed with the identical pipeline.

The *Rapidtide* commands are included in the GitHub repository listed earlier in this manuscript, and the input arguments used are summarized in Supplementary Table 1. These commands were run separately on the BH+REST and REST fMRI data segments for all subjects. Two *Rapidtide* output maps were extracted for further analysis (Figure 1B): the hemodynamic delay (temporal offset of the maximum correlation with the probe regressor, in seconds) and the correlation amplitude (maximum similarity function value, Pearson's r). *Rapidtide* resamples the probe regressor in each refinement step and produces correlation estimates on a continuous scale between the search range given. We chose a search range of –15 to +15 s to comfortably cover expected physiological ranges in a healthy cohort alongside using a data-driven probe regressor with no large offset. In our further analyses of delay values, we did not include any values at the boundary of this search range, deeming these not a true optimization and likely not physiologically plausible.

2.2.3 Hemodynamic delay comparison

The voxel-wise agreement between delay values from BH+REST and REST was calculated for all GM voxels using linear regression analysis, via the *polyfit* function in MATLAB (MATLAB and Statistics Toolbox Release 2021b, The MathWorks, Inc., Natick, Massachusetts, United States). This was repeated for subsets of GM voxels with increasing correlation amplitude thresholds applied (step=0.1, max 0.7): a voxel's correlation amplitude value had to pass the threshold in both BH+REST and REST data segments of a given subject to have the delay values included.

Three metrics were summarized: the spatial correlation coefficient, the slope of the linear regression model, and the percentage of voxels remaining after amplitude thresholding with respect to the entire GM. When the amplitude threshold is labeled as 'None' (e.g., x-axes in Figure 2), the percentage of voxels remaining is not at 100% because *Rapidtide* fails to produce a hemodynamic delay estimate for select GM voxels, resulting in the initial exclusion of these voxels from analysis. Figure 1C demonstrates the relationship between delay values at three different amplitude thresholds, for one example subject. All three metrics were then summarized across subjects using boxplots. The three metrics were also investigated within subregions of GM voxels. Using the MNI atlas described above, (Section 2.2.1), the same linear regression was performed for each GM atlas region (or parcel), then a median value across subjects was calculated for each metric, in order to easily visualize and compare the pattern of results between GM subregions.

2.2.4 Impact of spatial smoothing

Prior research using a lagged-GLM approach to map regional hemodynamic timings showed that these results were more robustly achieved in breath-hold versus resting-state data (Bright & Murphy, 2017; Stickland et al., 2021), likely due to the reduced signal-to-noise of respiratory-evoked vascular responses in resting-state data. To evaluate the role of signal-to-noise (SNR) limitations in the current results, we enhanced the degree of spatial filtering applied to the data prior to hemodynamic delay estimation, from σ = 1mm (FWHM 2.35mm, *Rapidtide* recommended setting for smoothing) to σ = 2.13mm (5mm FWHM). The same three metrics were calculated and compared with the original less-smoothed results.

3. Results

3.1 Hemodynamic delay agreement between breathing-task and resting-state data

Figure 1B displays amplitude and delay maps for one example subject, and maps for all subjects are presented in Supplementary Figure 1. For both BH+REST and REST data segments, correlation amplitude values were generally positive and show tissue contrast between GM and white matter (WM). Voxels with negative correlations, or where *Rapidtide* was not able to output a value, appear predominantly in or adjacent to the cerebrospinal fluid (CSF) and sometimes in WM; this is more notable for the REST data segment. The REST data segments also display lower correlation amplitudes across the brain compared to BH+REST, as anticipated. Delay maps show good GM/WM contrast for both data segments, although some voxel clusters of extreme values are present (see Discussion).

Figure 2 shows the summary of the three metrics used to assess hemodynamic delay agreement at different correlation amplitude thresholds: percentage voxels remaining, spatial correlation, and linear slope. As the amplitude threshold increases, fewer voxels remain, and the spatial correlation and slope of agreement relating the BH+REST vs REST hemodynamic delays both increase in a non-linear manner (Figure 1C, Figure 2, Supplementary Figure 2). In other words, the agreement between GM hemodynamic delay times in REST and BH+REST increases with stricter amplitude thresholding, as shown by the higher spatial correlation and the slope approaching a value of 1. Scatterplots comparing BH+REST and REST delay values for select amplitude thresholds are provided for all subjects (Supplementary Figure 2).

The parcellation analysis showed similar trends in each brain region examined (Figure 3). Except for the caudate, the spatial correlation and slope changed very similarly across amplitude thresholds, and every region except the caudate and cerebellum showed a notably large increase in spatial correlation strength between the amplitude thresholds of 0.4 and 0.5.

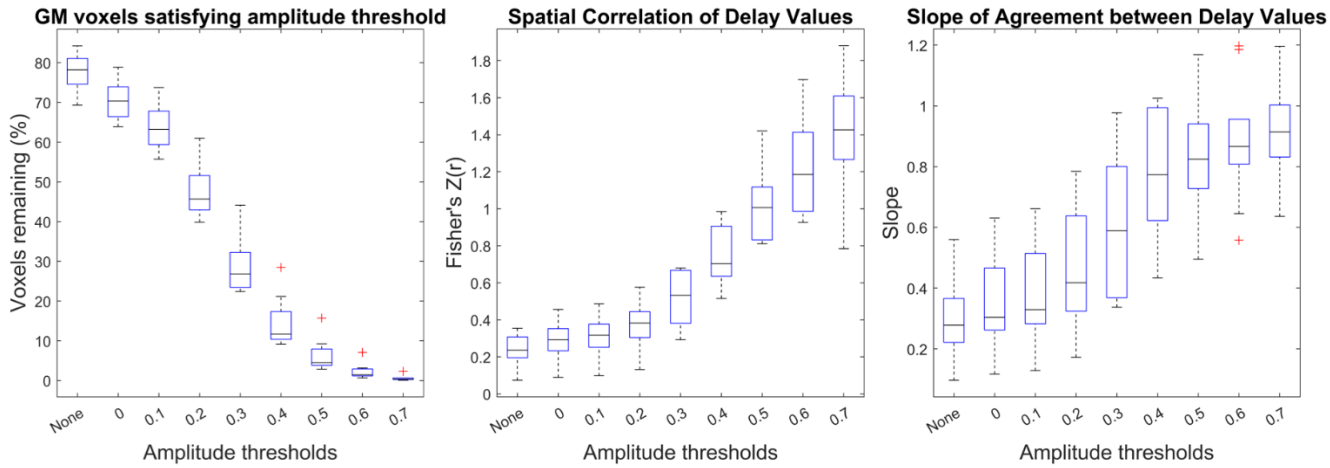

Figure 2. *Delay agreement between BH+REST and REST data segments within GM voxels, for each amplitude threshold. The boxplots summarize across subjects. The left plot shows the percentage of GM voxels satisfying each amplitude threshold in both data segments, where 'None' refers to no amplitude thresholding applied, and the subsequent numbers (0 to 0.7) refer to the amplitude threshold the voxel must exceed in order to be included in the assessment of delay agreement. The middle and right plots summarize the delay agreement for each amplitude threshold, showing the spatial correlation coefficients (middle plot) and slopes (right plot).*

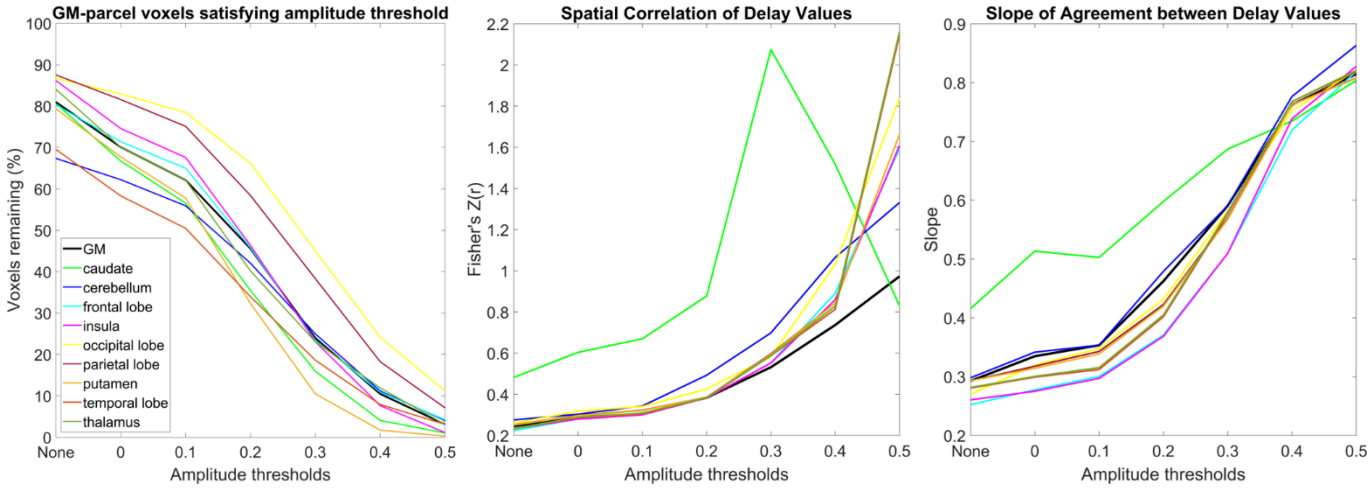

Figure 3. *Delay agreement between BH+REST and REST data segments within GM parcel voxels, for each amplitude threshold. These results are displayed in the same format as Figure 2 but display the median value across subjects for each GM parcel (colored lines) alongside the median value for total GM (black line), for visualization simplicity. The highest amplitude threshold that is summarized is capped at 0.5 because, for some GM parcels and some subjects, too few voxels pass the higher amplitude thresholds.*

After visualizing the spatial location of voxels passing high amplitude thresholds (0.6, 0.7), we noted their proximity to the sagittal sinus and other regions that are expected to have large venous blood vessel contributions to the fMRI signal (Figure 4). Based on this observation, we hypothesized that higher amplitude thresholds may isolate voxels reflecting larger veins rather than tissue. The voxel-wise Mean Signal Intensity (MSI) is partially reflective of local venous weighting: venous blood induces large signal dephasing, resulting in lower MSI across the functional BOLD-weighted images. These voxels may drive agreement between BH+REST and REST delay values, without faithfully representing tissue physiology.

To address this, we investigated the relationship between MSI and correlation amplitude threshold, hypothesizing the voxels passing the higher thresholds in both BH+REST and REST data segments would have lower MSI than the other thresholds, potentially due to the presence of larger veins. To visualize, MSI maps were overlayed with voxels passing the 0.6 amplitude threshold for both single subject and group data (Figure 4). Using the *ksdensity* function in MATLAB, the histograms of MSI values of voxels corresponding to each of the amplitude threshold bands 0-0.2, 0.2-0.4, 0.4-0.6, and larger or equal to 0.6 were extracted (Figure 4, with results from all subjects shown in Supplementary Figure 4). We observed that voxels with the highest correlation amplitudes in both data segments ($r > 0.6$) did generally reflect lower MSI values than other GM voxels, supporting our hypothesis that these voxels, at least in part, contain larger venous vessels.

To determine whether these voxels with very high correlation amplitudes drive the pattern of results presented in Figure 2, the original analysis was repeated for correlation amplitude bands rather than lower thresholds: 0 to 0.2, 0.2 to 0.4, and 0.4 to 0.6. Scatterplots showing these relationships are provided in Supplementary Figure 5. Figure 5 shows the summary of the three metrics used to assess hemodynamic delay, revealing similar trends to the original results: the spatial correlation increases and the slope increases, towards 1, with each increasing amplitude threshold band. Note that the percentage of voxels included in these threshold bands is small, indicating that many voxels show very different correlation amplitudes in the two data segments.

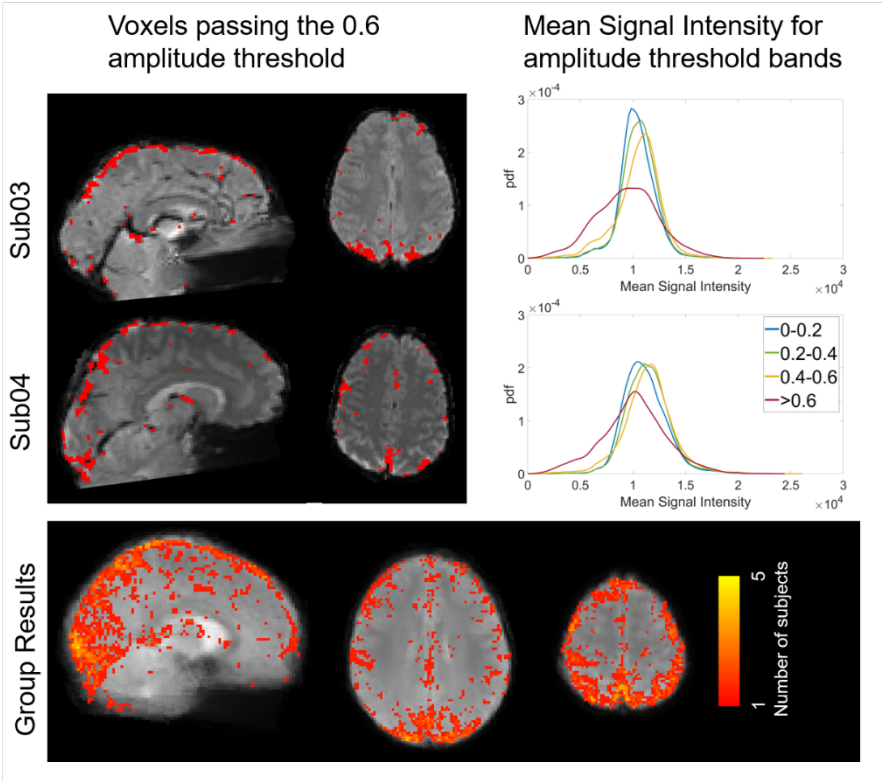

Figure 4. *Voxels passing the 0.6 amplitude threshold in both BH+REST and REST data segments overlaid on mean signal intensity (MSI) maps, and histograms showing MSI distributions for different amplitude threshold bands, for two example subjects and group-level summary. Example subject maps are in subject space and the group result maps are in MNI space.*

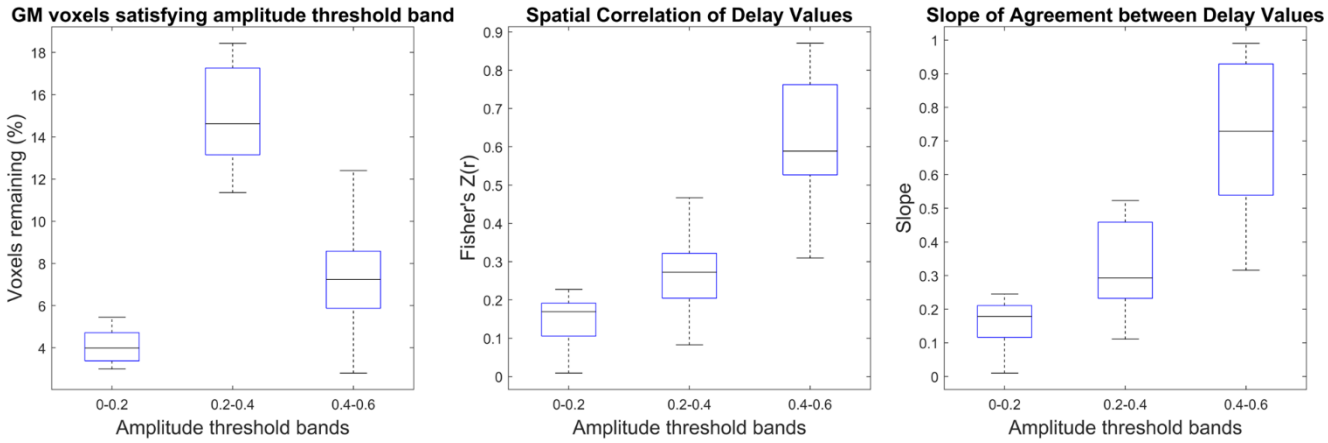

Figure 5. *Delay agreement between BH+REST and REST data segments within GM voxels, for each amplitude threshold band. The boxplots summarize across subjects. These results are displayed in the same format as Figure 2 (left: percentage of GM voxels satisfying each amplitude threshold, middle: spatial correlation coefficients, right: slopes) but instead of filtering the voxels with a single lower amplitude threshold, amplitude threshold bands are used (a voxel must be within the threshold band in both data segments to be included).*

3.2 Impact of Spatial Smoothing

Under additional spatial smoothing, we observe a widespread increase in correlation coefficient amplitudes (Figure 6) in both the BH+REST and REST data, which most likely reflects the improved signal-to-noise ratios achieved through this preprocessing step. Figure 7A demonstrates the effects of spatial smoothing on agreement between relative hemodynamic delay estimates, with the original results (median values from Figure 2) provided for comparison. Due to the increased correlation coefficient amplitudes in both data segments, the percentage of voxels remaining increased after additional smoothing. However, the spatial correlations of hemodynamic delays observed at each threshold are mostly unchanged. There is trend for better agreement (slope closer to 1) at lower amplitude thresholds in the additionally smoothed data (Figure 7A), however this is not readily interpretable given the inter-subject variability and the small sample size available. For the amplitude threshold band analysis after additional smoothing (Figure 7B), we see a different pattern in the voxel percentages in each threshold band. This corresponds to our observation that, with additional smoothing, more voxels pass higher amplitude thresholding. For this amplitude threshold band analysis, little difference in delay agreement, assessed with spatial correlation and slope, is observed after additional smoothing.

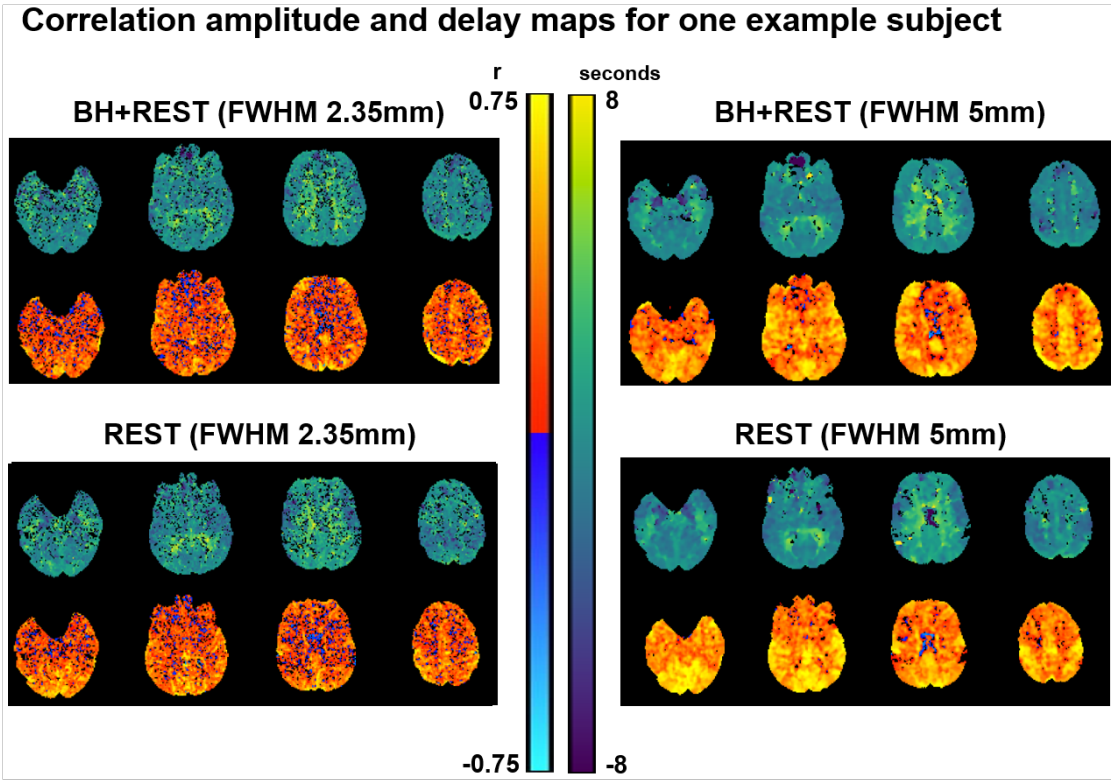

Figure 6. *Parameter maps generated with Rapidtide, for one example subject (sub01), before and after changing the level of smoothing. The top row displays the relative delays at each voxel (time in seconds when the maximum correlation occurred). The bottom displays the correlation amplitude at each voxel (maximum correlation coefficient between each voxel time-series and probe regressor).*

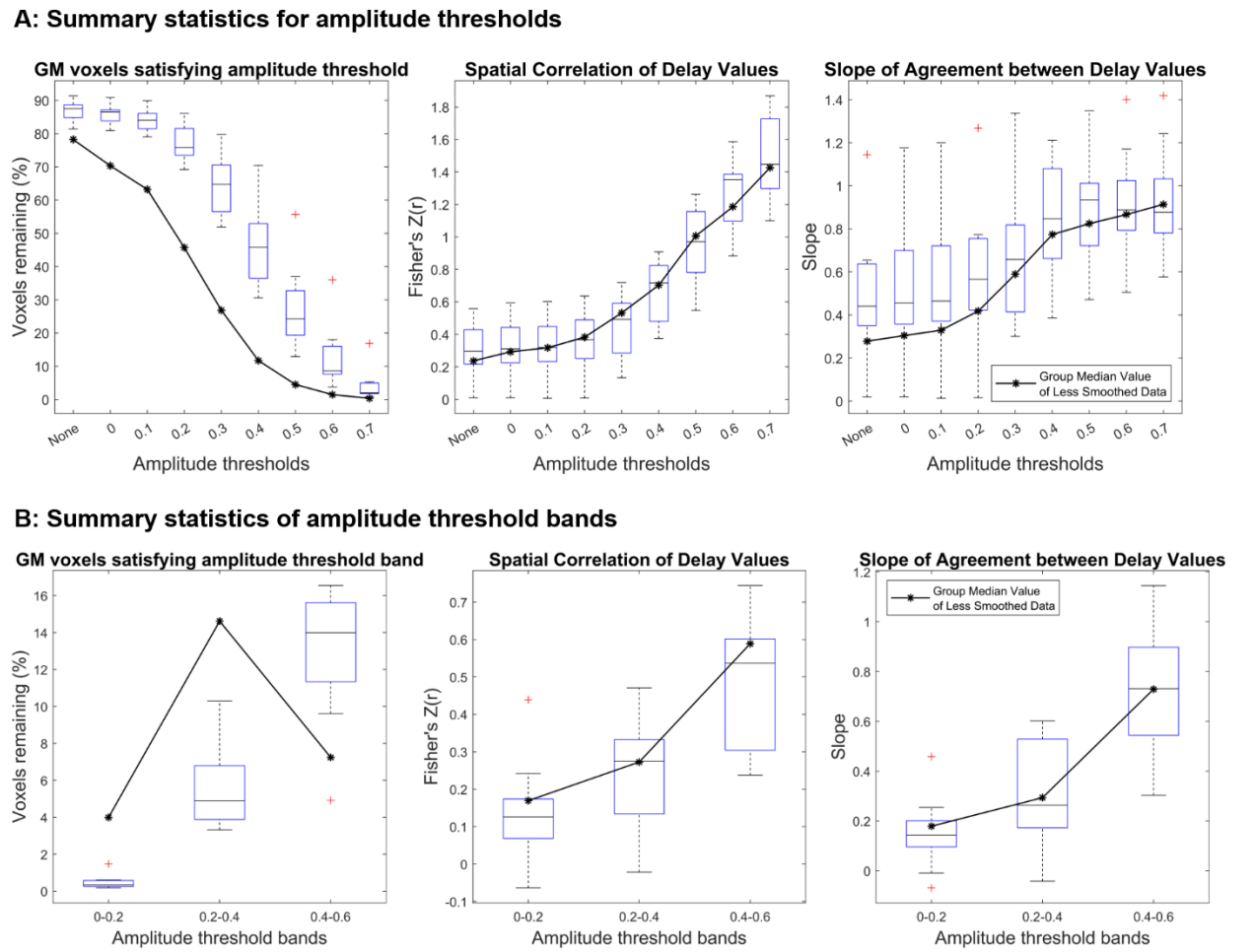

Figure 7. *Panel A and B summarize amplitude threshold and amplitude threshold band results, respectively, comparing the results with increased smoothing (FWHM 5mm) to the original results which had less smoothing (FWHM 2.35mm). The original results are shown as a black line for reference and duplicate the group median results from figures 2 and 5.*

4. Discussion

In BOLD-fMRI data containing a breath-hold task, we assume the globally driven vasodilatory effect dominates local hemodynamics, leading to a stronger relationship between a GM "probe" time-series and each voxel time-series. In comparison, in data containing only resting-state fluctuations, the signal amplitude and timing characteristics at each voxel will be more region-specific, influenced more by neurovascular factors which are not globally driven. In this study, we modeled resting-state and breathing-task data segments with an identical analytical pipeline, to assess whether they produced equivalent estimates of relative hemodynamic timings across cortical brain regions. As we applied stricter correlation amplitude thresholds (correlation between the voxel time-series and the probe regressor), including a smaller percentage of the total GM voxels with each new threshold applied, the spatial agreement of hemodynamic delays between BH+REST and REST increased. Broadly, the same pattern

of results was observed both when assessing all GM together and specific GM regions separately. We further observed that voxels passing the highest amplitude thresholds were more likely to be in closer proximity to venous structures; when removing these voxels from our analysis, we found similar trends to the original results, suggesting the delay agreement was not only driven by voxels proximal to large veins. Finally, applying additional smoothing to the input data boosted SNR and enhanced common variance shared across neighboring voxels; this produced widespread increases in correlation coefficient amplitudes, allowing more voxels to be included in the assessment of delay agreement, but did not meaningfully change the overall level of agreement for a given correlation amplitude. The subtleties of these results, alongside their limitations and implications, are further discussed.

4.1 Estimating hemodynamic delays

Our implementation of the *Rapidtide* toolbox estimated a delay value for the majority of voxels in the brain, with the only inputs being the fMRI data and a GM tissue mask generated from a T1-weighted image. Therefore, this is a feasible and accessible way for researchers to map hemodynamic delays and can be implemented with the imaging data alone (i.e., without the need for additional equipment or recordings). The majority of the *Rapidtide* settings we applied are default or recommended by the toolbox developers with some input arguments adapted specifically for the nature of our dataset and questions, as described in the methods section and Supplementary Table 1. In Tong et al., 2019, the *Rapidtide* authors explain some of the features of using a global mean signal as the probe regressor: it is simple to implement, does not require an externally derived regressor, and resembles the signal fluctuations of the superior sagittal sinus (aligned with our observations in Figure 4). This will be true for the GM average signal as well, which we used to define and refine the probe regressor in this study. We chose to focus on GM to match the voxels where agreement of hemodynamic delay values was assessed, acknowledging that GM tissue has the most relevance to fMRI analyses that rely on neurovascular coupling. Furthermore, we did not want timing differences between GM and WM voxels to dominate our assessment of agreement between data segments.

In fMRI analyses, the global signal has traditionally been used within the context of denoising, with the reasoning that it captures global "noise" rather than local neural "signal". However, its use is controversial considering the multitude of sources that can contribute to this signal (Liu, Nalci, & Falahpour, 2017). With the same logic that removing the global signal allows for the remaining variance to more closely resemble neural-driven mechanisms, specifically studying the global signal and its relationship to local signals can tell us more about non-neural hemodynamics. Tong et al (2019) discuss the challenges of using a data-driven mean signal regressor for both purposes; it is temporally "blurred" because it contains contributions from voxels with a range of delays and will also be influenced by local neural activity. To address these challenges *Rapidtide* implements a cross-correlation approach, often referred to as dynamic global signal regression in a denoising context (Erdogan et al., 2016). Within this cross-correlational approach, the *Rapidtide* algorithm goes through multiple analytical "passes", a bootstrapping method to improve the probe regressor and make it more closely resemble non-neural processes (see the flow chart

in Figure 5 of Tong et al., 2019). Further features, such as temporal filtering and iterative depseckling (using information from neighboring voxels to correct potentially bad delay estimates) are also applied. Please refer to Tong et al (2019) and the *Rapidtide* documentation (Frederick, 2016-2022) for more details and a more in-depth discussion of how voxel-wise hemodynamic delays are estimated and interpreted within this software package.

From visual inspection, the *Rapidtide* amplitude and delay maps broadly agree with previous CVR literature in healthy cohorts using resting-state or breathing-task designs, showing contrast between GM and WM tissue (Moia et al., 2021; Stickland et al., 2021; Tong et al., 2019), with negative CVR-related correlation amplitudes scattered more commonly across WM than GM but mostly clustered adjacent to CSF (Bright, Bianciardi, de Zwart, Murphy, & Duyn, 2014; Thomas et al., 2013). For some subjects, the delay maps contain clusters of extreme delay values (Supplementary Figures 1 and 6). Obvious explanations are unclear, but the *Rapidtide* despeckling procedure, and the smoothing we applied, could have accentuated these extreme clusters. They are present in both data segments but are more prominent in the REST data segment. Considering some of these regionally specific extreme delays, we also investigated the relationship between delay values at the level of GM cortical parcels. This allowed us to assess whether it was valid to summarize the patterns of agreement in delay at the level of the whole GM, or if different brain regions displayed notably different patterns of agreement across amplitude thresholds. However, we did not observe a meaningful difference in hemodynamic delay agreement across cortical regions.

4.2 Assessing the agreement of hemodynamic delays at different amplitude thresholds

For all subjects, we see positive correlations and slopes between BH+REST and REST data segments, at every amplitude threshold. The median slope across subjects, for every amplitude threshold, is below 1. This suggests a larger range of delay estimates in the data segment containing the breathing-task compared to the data segment containing resting fluctuations only. The results and relationships we observe across all GM voxels are consistent with those observed in the smaller GM subregions. The caudate is the only region that notably deviates from the others, perhaps due to its small size, as there are more partial volume effects and noisy voxels affecting summary timing estimates.

Further work is needed to concretely establish the reasons for (dis)agreement between hemodynamic delays measured in the breathing-task and resting-state data; are the relationships we observe driven by methodology, physiology, or both? We attempted to explore these questions by assessing how the agreement changed when: (1) restricting the voxels included (via amplitude thresholds), (2) investigating specific voxels that may have a strong influence on the overall agreement and (3) changing the signal-to-noise ratio of the input data via increased spatial smoothing.

Firstly, if we examine the agreement of delay values with no amplitude threshold applied, therefore including most of the GM voxels within the linear model, we see very low correlations and slopes of 0.278 and 0.440 (median across subjects, less-smoothed and more-smoothed analysis, respectively). Moderate to strong correlations, with slopes closer to one, are only achieved when including a very small percentage of GM voxels, the voxels with the strongest positive correlation with the probe regressor. It is more difficult to interpret slopes when the correlation values are low, however the monotonic increase of correlation and slope, as amplitude threshold increases, is interesting to reflect on. With these results, we cannot conclude that the delay values estimated with resting-state and with breathing-task data have the same physiological meaning in every voxel; estimates may only converge when the weighting of neural, vascular and other physiological factors are the same. The improved delay agreement with higher amplitude thresholding may also reflect improved SNR, where higher correlation amplitudes make the measurement of hemodynamic delay more robust in the presence of other ongoing signal processes ("noise").

Secondly, our results suggest that voxels with the strongest relationship with the probe regressor (in both data segments) are located close to the sagittal sinus and other regions that are expected to have large venous blood contributions. A similar observation was noted by a different group of researchers (Tong, Bergethon, & Frederick, 2011); they found, as have others, that the largest BOLD CVR-related amplitude changes are in large blood vessels, and that signal amplitude changes were most similar between a resting-state and a breath-hold dataset in these large vessels compared to in other regions. We went on to exclude these voxels in an attempt to assess hemodynamic delays relevant to local physiology, not just global vascular drainage. Without the inclusion of these high-amplitude voxels, we still observe a monotonic increase of spatial correlation and slope with each increasing amplitude threshold band. To compare further, we can examine the spatial correlation and slope values for the 0.4 amplitude threshold (Figure 2) and the same values from the 0.4-0.6 amplitude threshold band (Figure 5). In Figure 2, all values 0.4 and above are included, whereas in Figure 5 this is capped at 0.6, thus excluding many voxels capturing large veins. The median spatial correlation across subjects is slightly larger in Figure 2 compared to Figure 5 for these thresholds (0.7031 vs. 0.5886) as well as the median slope (0.7738 vs. 0.7291). This small difference in correlation and slope that could be explained by the rarity of voxels passing the 0.6 amplitude threshold. However, it also indicates that voxels with large venous vessels drive some of the agreement seen, but likely not all. Larger samples, and data acquisitions more tailored towards identifying venous weighting, would be needed to understand if this is meaningful.

Finally, increased smoothing of the input data increased the amplitude correlation coefficients of GM voxels on average (i.e., increased their correlation strength with the probe regressor). This is likely because of a reduced contribution from neurovascular fluctuations specific to each voxel, as well as other sources of local fMRI noise, leaving more shared features between neighboring voxels. This increased smoothing allowed more GM voxels to be included in the assessment of delay agreement for every amplitude threshold and manifested in similar or slightly improved hemodynamic delay agreement between the resting-state and breathing-task datasets. Therefore, this

suggests that SNR factors do play a role in the agreement of delay estimates, and this is also consistent with the idea that higher agreement is observed in voxels with a stronger relationship to the global probe regressor. However, smoothing the data also amplified some unusual disagreement in hemodynamic delay observed in select subjects. For example, the scatterplots for Subject 3 in Supplementary Figures 2A and 7 demonstrate that there are select groups of voxels with near-zero hemodynamic delay in the BH+REST data but much more extreme relative delays in the REST data segment. (Note that this phenomenon appears limited to a small number of voxels, and it is counter to our observation, described above, that breathing-task data generally produces a wider range of delay values across all GM.) Such disagreement could suggest that the *Rapidtide* algorithm is problematically impacted by other ongoing signal fluctuations present in resting-state data that have distinct dynamics to low-frequency systemic vasodilatory effects and are coordinated across multiple contiguous voxels. In contrast, the higher SNR and greater specificity to CO_2-related vasodilatory effects that are achieved by having a breathing task may prevent this fitting challenge, irrespective of spatial smoothing.

4.3 Alternative breathing tasks

As an alternative to the BH task which induces hypercapnia, the neuroimaging dataset also included a cued deep breathing (CDB) task in the same participants, which induces hypocapnia via hyperventilation, described in (Stickland et al., 2021). Two repetitions of fast deep breaths were cued, and an 8-minute rest period followed this CDB task. As with the BH+REST dataset, two equal-length data segments were extracted. We replicated the main analysis with this alternative breathing task (the agreement of hemodynamic timings between CDB+REST and REST, across amplitude thresholds), shown in Supplementary Figures 2B and 3. Except for one subject being removed from group summaries as an outlier, we note the same trends and key findings reported in the main manuscript with the BH+REST dataset. Although our observations may be fairly robust to the breathing task used, we note that this may not be true in patients with vascular pathology; altered baseline vascular tone can differentially impact hypercapnic and hypocapnic cerebrovascular reactivity, including both the magnitude and delay of the vascular response (Bright, Donahue, Duyn, Jezzard, & Bulte, 2011; Zhao et al., 2009).

4.4 Alternative approaches to estimating hemodynamic delays

There are alternative approaches to estimating hemodynamic delays with BOLD-fMRI data, each with their pros and cons relating to complexity of acquisition and analysis. Using probe regressors external to the brain such as end-tidal CO_2 or near-infrared spectroscopy (Pinto et al., 2016; Tong et al., 2019), instead of a data-driven regressor, results in the regression coefficients having a more specific physiological interpretation and being easier to compare across studies. This is a more important priority when scaling BOLD amplitude changes, rather than timing; timing

estimates are often normalized to a common spatial reference (i.e., median timing across gray matter voxels, as done in this paper) even when an external probe regressor is used. Furthermore, we previously found that when using an external end-tidal CO_2 regressor within a lagged general linear model framework it can be challenging to get trustworthy estimates of delay in resting-state data alone (Bright, Tench, & Murphy, 2017; Stickland et al., 2021). Other modeling approaches exist to extract timing information, for example, Fourier based analyses (Pinto et al., 2016), but without a signal model for the resting-state data, this cannot be applied in the same way as with a breathing task or gas delivery design with a specific task frequency. Compared to our task paradigm, previous papers using breathing tasks will typically employ more repeated breath-hold cycles to improve the modeling of vascular reactivity mechanisms, and it is recommended to use multi-echo BOLD fMRI data with spatial ICA-denoising to better remove motion artifacts (Cohen & Wang, 2019; Moia et al., 2021). These factors should be considered to improve future comparisons of BOLD timing estimates from resting-state and breathing-task designs.

4.5 Limitations and further considerations

The two data segments compared in this manuscript, BH+REST and REST, overlapped in time (Figure 1A). It could be argued that this would lead to artificial agreement when trying to compare 'breathing-task' data to 'resting-state' data; though this may be the case, our results show that good agreement of hemodynamic timings is only achieved under relatively strict analytical constraints, even with this overlap. Looking at Supplementary Figures 1 and 6, there are many clusters of voxels that show divergent hemodynamic delay estimates in BH+REST compared to REST (for example see subjects 07, 09, and 10), and much of the analysis we performed attempted to understand this disagreement. The advantages of using overlapping time segments include fewer confounding factors due to the participant being in a different physiological state. Furthermore, using two different sections of the same scan means sources of error driven by volume registration are minimized, making the voxelwise comparisons more valid. This allowed us to more confidently interpret any differences in hemodynamic timing estimates as driven by replacing a resting-state portion of the dataset with a hypercapnic breathing task portion.

Although the timing and the shape of the blood flow response have been shown to be different under different arterial blood gas conditions (Birn, Smith, Jones, & Bandettini, 2008; Donahue et al., 2014; Kasprowicz et al., 2012), it is hard to directly apply these findings to the interpretation of our local hemodynamic delays being that our delay values are estimated from time-series analyses and are relative to two different data-driven probe regressors. With our data and analysis methodology, we cannot specifically quantify arterial arrival times or blood flow changes in response to a known change in arterial blood gas tensions. However, when correcting fMRI analyses and bringing clinical insight to regional cerebrovascular dysfunction, it is likely that relative hemodynamic timings are sufficient.

Finally, this study has a small sample size, and future work should investigate these questions further with larger and more diverse samples to determine generalizability. Additional data in patient cohorts with atypical regional hemodynamics would also help confirm the interpretation of our results. We provide many supplementary figures to complement the main results, in order to transparently communicate the full data variance in this healthy cohort.

5. Conclusions

We modeled BOLD fMRI data to estimate relative hemodynamic delay values across the brain, focusing on GM tissue. We investigated how these delay estimates change in the presence of a breathing-task versus in resting-state data. Hemodynamic delay information is a clinically meaningful marker of cerebrovascular function, as well as being important for correcting hemodynamic biases in task-based and FC fMRI analyses. We found strong similarities between estimates from resting-state data and breathing-task data only when strict amplitude thresholds are applied, comparing a small percentage of GM voxels. A stronger agreement between delays estimated in these two different data types was seen in voxels that more closely resembled the global GM average, and localized (at least in part) to large venous structures. Caution must be taken when using voxel-wise delay estimates from resting-state and breathing-task data interchangeably, and further work is needed to more directly identify the local and global signal contributions that lead to their disagreement.

Acknowledgments

The authors thank the members of the Applied Neuro-Vascular Imaging Lab (ANVIL) at Northwestern University for their generous support on the revision of the manuscript and figures. This work was supported by the Center for Translational Imaging at Northwestern University. We also want to express our special thanks to Dr. Blaise Frederick for his assistance implementing the *Rapidtide* software package.

Funding

This research was supported by the Eunice Kennedy Shriver National Institute of Child Health and Human Development of the National Institutes of Health under award number K12HD073945. JG was supported by multiple grants from the Northwestern University Office of Undergraduate Research, Robert R. McCormick School of Engineering and Applied Science, and Department of Biomedical Engineering. The conclusions, opinions, and other statements in this presentation are the author's and not necessarily those of the sponsoring institution.

References

Birn, R. M., Smith, M. A., Jones, T. B., & Bandettini, P. A. (2008). The respiration response function: the temporal dynamics of fMRI signal fluctuations related to changes in respiration. *Neuroimage, 40*(2), 644-654. doi:10.1016/j.neuroimage.2007.11.059

Bright, M. G., Bianciardi, M., de Zwart, J. A., Murphy, K., & Duyn, J. H. (2014). Early anti-correlated BOLD signal changes of physiologic origin. *Neuroimage, 87*, 287-296. doi:10.1016/j.neuroimage.2013.10.055

Bright, M. G., Bulte, D. P., Jezzard, P., & Duyn, J. H. (2009). Characterization of regional heterogeneity in cerebrovascular reactivity dynamics using novel hypocapnia task and BOLD fMRI. *Neuroimage, 48*(1), 166-175. doi:10.1016/j.neuroimage.2009.05.026

Bright, M. G., Donahue, M. J., Duyn, J. H., Jezzard, P., & Bulte, D. P. (2011). The effect of basal vasodilation on hypercapnic and hypocapnic reactivity measured using magnetic resonance imaging. *J Cereb Blood Flow Metab, 31*(2), 426-438. doi:10.1038/jcbfm.2010.187

Bright, M. G., & Murphy, K. (2017). Cleaning up the fMRI time series: Mitigating noise with advanced acquisition and correction strategies. *Neuroimage, 154*, 1-3. doi:10.1016/j.neuroimage.2017.03.056

Bright, M. G., Tench, C. R., & Murphy, K. (2017). Potential pitfalls when denoising resting state fMRI data using nuisance regression. *Neuroimage, 154*, 159-168. doi:10.1016/j.neuroimage.2016.12.027

Caballero-Gaudes, C., & Reynolds, R. C. (2017). Methods for cleaning the BOLD fMRI signal. *Neuroimage, 154*, 128-149. doi:10.1016/j.neuroimage.2016.12.018

Cai, S., Shi, Z., Zhou, S., Liang, Y., Wang, L., Wang, K., & Zhang, L. (2022). Cerebrovascular Dysregulation in Patients with Glioma Assessed with Time-shifted BOLD fMRI. *Radiology, 304*(1), 155-163. doi:10.1148/radiol.212192

Champagne, A. A., Coverdale, N. S., Allen, M. D., Tremblay, J. C., MacPherson, R. E. K., Pyke, K. E., . . . Cook, D. J. (2022). The physiological basis underlying functional connectivity differences in older adults: A multi-modal analysis of resting-state fMRI. *Brain Imaging Behav, 16*(4), 1575-1591. doi:10.1007/s11682-021-00570-0

Chang, C., Thomason, M. E., & Glover, G. H. (2008). Mapping and correction of vascular hemodynamic latency in the BOLD signal. *Neuroimage, 43*(1), 90-102. doi:10.1016/j.neuroimage.2008.06.030

Chang, T. Y., Kuan, W. C., Huang, K. L., Chang, C. H., Chang, Y. J., Wong, H. F., . . . Liu, H. L. (2013). Heterogeneous cerebral vasoreactivity dynamics in patients with carotid stenosis. *PLoS One, 8*(9), e76072. doi:10.1371/journal.pone.0076072

Chen, J. J., & Gauthier, C. J. (2021). The Role of Cerebrovascular-Reactivity Mapping in Functional MRI: Calibrated fMRI and Resting-State fMRI. *Front Physiol, 12*, 657362. doi:10.3389/fphys.2021.657362

Chi, N. F., Ku, H. L., Chen, D. Y., Tseng, Y. C., Chen, C. J., Lin, Y. C., . . . Hu, C. J. (2018). Cerebral Motor Functional Connectivity at the Acute Stage: An Outcome Predictor of Ischemic Stroke. *Sci Rep, 8*(1), 16803. doi:10.1038/s41598-018-35192-y

Cohen, A. D., & Wang, Y. (2019). Improving the Assessment of Breath-Holding Induced Cerebral Vascular Reactivity Using a Multiband Multi-echo ASL/BOLD Sequence. *Sci Rep, 9*(1), 5079. doi:10.1038/s41598-019-41199-w

Cohen, E. R., Ugurbil, K., & Kim, S. G. (2002). Effect of basal conditions on the magnitude and dynamics of the blood oxygenation level-dependent fMRI response. *J Cereb Blood Flow Metab, 22*(9), 1042-1053. doi:10.1097/00004647-200209000-00002

Collins, D. L., Holmes, C. J., Peters, T. M., & Evans, A. C. (1995). Automatic 3-D model-based neuroanatomical segmentation. *Human Brain Mapping, 3*(3), 190-208. doi:https://doi.org/10.1002/hbm.460030304

Donahue, M. J., Faraco, C. C., Strother, M. K., Chappell, M. A., Rane, S., Dethrage, L. M., . . . Siero, J. C. (2014). Bolus arrival time and cerebral blood flow responses to hypercarbia. *J Cereb Blood Flow Metab, 34*(7), 1243-1252. doi:10.1038/jcbfm.2014.81

Donahue, M. J., Strother, M. K., Lindsey, K. P., Hocke, L. M., Tong, Y., & Frederick, B. D. (2016). Time delay processing of hypercapnic fMRI allows quantitative parameterization of cerebrovascular reactivity and blood flow delays. *J Cereb Blood Flow Metab, 36*(10), 1767-1779. doi:10.1177/0271678X15608643

Erdogan, S. B., Tong, Y., Hocke, L. M., Lindsey, K. P., & Frederick, B. (2016). Correcting for Blood Arrival Time in Global Mean Regression Enhances Functional Connectivity Analysis of Resting State fMRI-BOLD Signals. *Front Hum Neurosci, 10*, 311. doi:10.3389/fnhum.2016.00311

Fesharaki, N. J., Mathew, A. B., Mathis, J. R., Huddleston, W. E., Reuss, J. L., Pillai, J. J., & DeYoe, E. A. (2021). Effects of Thresholding on Voxel-Wise Correspondence of Breath-Hold and Resting-State Maps of Cerebrovascular Reactivity. *Front Neurosci, 15*, 654957. doi:10.3389/fnins.2021.654957

Frederick, B. B., Rapidtide. [Computer Program] (2016-2022). Retrieved from https://github.com/bbfrederick/rapidtide. doi:10.5281/zenodo.814990

Friston, K. J., Fletcher, P., Josephs, O., Holmes, A., Rugg, M. D., & Turner, R. (1998). Event-related fMRI: characterizing differential responses. *Neuroimage, 7*(1), 30-40. doi:10.1006/nimg.1997.0306

Geranmayeh, F., Wise, R. J., Leech, R., & Murphy, K. (2015). Measuring vascular reactivity with breath-holds after stroke: a method to aid interpretation of group-level BOLD signal changes in longitudinal fMRI studies. *Hum Brain Mapp, 36*(5), 1755-1771. doi:10.1002/hbm.22735

Glover, G. H. (2011). Overview of functional magnetic resonance imaging. *Neurosurg Clin N Am, 22*(2), 133-139, vii. doi:10.1016/j.nec.2010.11.001

Handwerker, D. A., Gazzaley, A., Inglis, B. A., & D'Esposito, M. (2007). Reducing vascular variability of fMRI data across aging populations using a breathholding task. *Hum Brain Mapp, 28*(9), 846-859. doi:10.1002/hbm.20307

Handwerker, D. A., Ollinger, J. M., & D'Esposito, M. (2004). Variation of BOLD hemodynamic responses across subjects and brain regions and their effects on statistical analyses. *Neuroimage, 21*(4), 1639-1651. doi:10.1016/j.neuroimage.2003.11.029

Holmes, K. R., Tang-Wai, D., Sam, K., McKetton, L., Poublanc, J., Crawley, A. P., . . . Mikulis, D. J. (2020). Slowed Temporal and Parietal Cerebrovascular Response in Patients with Alzheimer's Disease. *Can J Neurol Sci, 47*(3), 366-373. doi:10.1017/cjn.2020.30

Hu, J. Y., Kirilina, E., Nierhaus, T., Ovadia-Caro, S., Livne, M., Villringer, K., . . . Khalil, A. A. (2021). A novel approach for assessing hypoperfusion in stroke using spatial independent component analysis of resting-state fMRI. *Hum Brain Mapp, 42*(16), 5204-5216. doi:10.1002/hbm.25610

Huneau, C., Benali, H., & Chabriat, H. (2015). Investigating Human Neurovascular Coupling Using Functional Neuroimaging: A Critical Review of Dynamic Models. *Front Neurosci, 9*, 467. doi:10.3389/fnins.2015.00467

Issard, C., & Gervain, J. (2018). Variability of the hemodynamic response in infants: Influence of experimental design and stimulus complexity. *Dev Cogn Neurosci, 33*, 182-193. doi:10.1016/j.dcn.2018.01.009

Jahanian, H., Christen, T., Moseley, M. E., & Zaharchuk, G. (2018). Erroneous Resting-State fMRI Connectivity Maps Due to Prolonged Arterial Arrival Time and How to Fix Them. *Brain Connect, 8*(6), 362-370. doi:10.1089/brain.2018.0610

Jenkinson, M., Bannister, P., Brady, M., & Smith, S. (2002). Improved optimization for the robust and accurate linear registration and motion correction of brain images. *Neuroimage, 17*(2), 825-841. doi:10.1016/s1053-8119(02)91132-8

Jenkinson, M., Beckmann, C. F., Behrens, T. E., Woolrich, M. W., & Smith, S. M. (2012). Fsl. *Neuroimage, 62*(2), 782-790. doi:10.1016/j.neuroimage.2011.09.015

Jenkinson, M., & Smith, S. (2001). A global optimisation method for robust affine registration of brain images. *Med Image Anal, 5*(2), 143-156. doi:10.1016/s1361-8415(01)00036-6

Kannurpatti, S. S., & Biswal, B. B. (2008). Detection and scaling of task-induced fMRI-BOLD response using resting state fluctuations. *Neuroimage, 40*(4), 1567-1574. doi:10.1016/j.neuroimage.2007.09.040

Kasprowicz, M., Diedler, J., Reinhard, M., Carrera, E., Steiner, L. A., Smielewski, P., . . . Czosnyka, M. (2012). Time constant of the cerebral arterial bed in normal subjects. *Ultrasound Med Biol, 38*(7), 1129-1137. doi:10.1016/j.ultrasmedbio.2012.02.014

Kötter, R., Mazziotta, J., Toga, A., Evans, A., Fox, P., Lancaster, J., . . . Mazoyer, B. (2001). A probabilistic atlas and reference system for the human brain: International Consortium for Brain Mapping (ICBM). *Philosophical Transactions of the Royal Society of London. Series B: Biological Sciences, 356*(1412), 1293-1322. doi:doi:10.1098/rstb.2001.0915

Leung, J., Duffin, J., Fisher, J. A., & Kassner, A. (2016). MRI-based cerebrovascular reactivity using transfer function analysis reveals temporal group differences between patients with sickle cell disease and healthy controls. *Neuroimage Clin, 12*, 624-630. doi:10.1016/j.nicl.2016.09.009

Li, X., Morgan, P. S., Ashburner, J., Smith, J., & Rorden, C. (2016). The first step for neuroimaging data analysis: DICOM to NIfTI conversion. *J Neurosci Methods, 264*, 47-56. doi:10.1016/j.jneumeth.2016.03.001

Li, Y. T., Wu, P. Y., Lu, J. T. Y., Chu, Y. H., Hsu, Y. C., & Lin, F. H. (2018). Inter-Regional BOLD Latency after Vascular Reactivity Calibration is Correlated to Reaction Time. *ISMRM Abstract, 0148*.

Lipp, I., Murphy, K., Caseras, X., & Wise, R. G. (2015). Agreement and repeatability of vascular reactivity estimates based on a breath-hold task and a resting state scan. *Neuroimage, 113*, 387-396. doi:10.1016/j.neuroimage.2015.03.004

Liu, P., De Vis, J. B., & Lu, H. (2019). Cerebrovascular reactivity (CVR) MRI with CO2 challenge: A technical review. *Neuroimage, 187*, 104-115. doi:10.1016/j.neuroimage.2018.03.047

Liu, P., Li, Y., Pinho, M., Park, D. C., Welch, B. G., & Lu, H. (2017). Cerebrovascular reactivity mapping without gas challenges. *Neuroimage, 146*, 320-326. doi:10.1016/j.neuroimage.2016.11.054

Liu, T. T. (2013). Neurovascular factors in resting-state functional MRI. *Neuroimage, 80*, 339-348. doi:10.1016/j.neuroimage.2013.04.071

Liu, T. T. (2016). Noise contributions to the fMRI signal: An overview. *Neuroimage, 143*, 141-151. doi:10.1016/j.neuroimage.2016.09.008

Liu, T. T., Behzadi, Y., Restom, K., Uludag, K., Lu, K., Buracas, G. T., . . . Buxton, R. B. (2004). Caffeine alters the temporal dynamics of the visual BOLD response. *Neuroimage, 23*(4), 1402-1413. doi:10.1016/j.neuroimage.2004.07.061

Liu, T. T., Nalci, A., & Falahpour, M. (2017). The global signal in fMRI: Nuisance or Information? *Neuroimage, 150*, 213-229. doi:10.1016/j.neuroimage.2017.02.036

Magon, S., Basso, G., Farace, P., Ricciardi, G. K., Beltramello, A., & Sbarbati, A. (2009). Reproducibility of BOLD signal change induced by breath holding. *Neuroimage, 45*(3), 702-712. doi:10.1016/j.neuroimage.2008.12.059

Martindale, J., Mayhew, J., Berwick, J., Jones, M., Martin, C., Johnston, D., . . . Zheng, Y. (2003). The hemodynamic impulse response to a single neural event. *J Cereb Blood Flow Metab, 23*(5), 546-555. doi:10.1097/01.WCB.0000058871.46954.2B

Moia, S., Stickland, R. C., Ayyagari, A., Termenon, M., Caballero-Gaudes, C., & Bright, M. G. (2020). Voxelwise optimization of hemodynamic lags to improve regional CVR estimates in breath-hold fMRI. *42nd Annual International Conference of the IEEE Engineering in Medicine & Biology Society (EMBC)*, 1489-1492.

Moia, S., Termenon, M., Urunuela, E., Chen, G., Stickland, R. C., Bright, M. G., & Caballero-Gaudes, C. (2021). ICA-based denoising strategies in breath-hold induced cerebrovascular reactivity mapping with multi echo BOLD fMRI. *Neuroimage, 233*, 117914. doi:10.1016/j.neuroimage.2021.117914

Murphy, K., Birn, R. M., & Bandettini, P. A. (2013). Resting-state fMRI confounds and cleanup. *Neuroimage, 80*, 349-359. doi:10.1016/j.neuroimage.2013.04.001

Murphy, K., Harris, A. D., & Wise, R. G. (2011). Robustly measuring vascular reactivity differences with breath-hold: normalising stimulus-evoked and resting state BOLD fMRI data. *Neuroimage, 54*(1), 369-379. doi:10.1016/j.neuroimage.2010.07.059

Ni, L., Li, J., Li, W., Zhou, F., Wang, F., Schwarz, C. G., . . . Xu, Y. (2017). The value of resting-state functional MRI in subacute ischemic stroke: comparison with dynamic susceptibility contrast-enhanced perfusion MRI. *Sci Rep, 7*, 41586. doi:10.1038/srep41586

Penny, W., Friston, K., Ashburner, J., Kiebel, S., & Nichols, T. (2006). Statistical Parametric Mapping (SPM12) [MATLAB Toolbox]. London. Retrieved from www.fil.ion.ucl.ac.uk/spm

Pinto, J., Bright, M. G., Bulte, D. P., & Figueiredo, P. (2020). Cerebrovascular Reactivity Mapping Without Gas Challenges: A Methodological Guide. *Front Physiol, 11*, 608475. doi:10.3389/fphys.2020.608475

Pinto, J., Jorge, J., Sousa, I., Vilela, P., & Figueiredo, P. (2016). Fourier modeling of the BOLD response to a breath-hold task: Optimization and reproducibility. *Neuroimage, 135*, 223-231. doi:10.1016/j.neuroimage.2016.02.037

Raut, R. V., Nair, V. A., Sattin, J. A., & Prabhakaran, V. (2016). Hypercapnic evaluation of vascular reactivity in healthy aging and acute stroke via functional MRI. *Neuroimage Clin, 12*, 173-179. doi:10.1016/j.nicl.2016.06.016

Siegel, J. S., Snyder, A. Z., Ramsey, L., Shulman, G. L., & Corbetta, M. (2016). The effects of hemodynamic lag on functional connectivity and behavior after stroke. *J Cereb Blood Flow Metab, 36*(12), 2162-2176. doi:10.1177/0271678X15614846

Sleight, E., Stringer, M. S., Marshall, I., Wardlaw, J. M., & Thrippleton, M. J. (2021). Cerebrovascular Reactivity Measurement Using Magnetic Resonance Imaging: A Systematic Review. *Front Physiol, 12*, 643468. doi:10.3389/fphys.2021.643468

Smith, S. M. (2002). Fast robust automated brain extraction. *Hum Brain Mapp, 17*(3), 143-155. doi:10.1002/hbm.10062

Smith, S. M., Jenkinson, M., Woolrich, M. W., Beckmann, C. F., Behrens, T. E., Johansen-Berg, H., . . . Matthews, P. M. (2004). Advances in functional and structural MR image analysis and implementation as FSL. *Neuroimage, 23 Suppl 1*, S208-219. doi:10.1016/j.neuroimage.2004.07.051

Sousa, I., Vilela, P., & Figueiredo, P. (2014). Reproducibility of hypocapnic cerebrovascular reactivity measurements using BOLD fMRI in combination with a paced deep breathing task. *Neuroimage, 98*, 31-41. doi:10.1016/j.neuroimage.2014.04.049

Stickland, R. C., Bright, M. G., Moia, S., & Zvolanek, K. M., Breathing-Task-Visual-PsychoPy. [Computer Program] (2022). doi:10.5281/zenodo.7056657

Stickland, R. C., Zvolanek, K. M., Moia, S., Ayyagari, A., Caballero-Gaudes, C., & Bright, M. G. (2021). A practical modification to a resting state fMRI protocol for improved characterization of cerebrovascular function. *Neuroimage, 239*, 118306. doi:10.1016/j.neuroimage.2021.118306

Thomas, B. P., Liu, P., Aslan, S., King, K. S., van Osch, M. J., & Lu, H. (2013). Physiologic underpinnings of negative BOLD cerebrovascular reactivity in brain ventricles. *Neuroimage, 83*, 505-512. doi:10.1016/j.neuroimage.2013.07.005

Thomason, M. E., Foland, L. C., & Glover, G. H. (2007). Calibration of BOLD fMRI using breath holding reduces group variance during a cognitive task. *Hum Brain Mapp, 28*(1), 59-68. doi:10.1002/hbm.20241

Tisdall, M. D., Reuter, M., Qureshi, A., Buckner, R. L., Fischl, B., & van der Kouwe, A. J. W. (2016). Prospective motion correction with volumetric navigators (vNavs) reduces the bias and variance in brain morphometry induced by subject motion. *Neuroimage, 127*, 11-22. doi:10.1016/j.neuroimage.2015.11.054

Tong, Y., Bergethon, P. R., & Frederick, B. D. (2011). An improved method for mapping cerebrovascular reserve using concurrent fMRI and near-infrared spectroscopy with Regressor Interpolation at Progressive Time Delays (RIPTiDe). *Neuroimage, 56*(4), 2047-2057. doi:10.1016/j.neuroimage.2011.03.071

Tong, Y., Hocke, L. M., & Frederick, B. B. (2019). Low Frequency Systemic Hemodynamic "Noise" in Resting State BOLD fMRI: Characteristics, Causes, Implications, Mitigation Strategies, and Applications. *Front Neurosci, 13*, 787. doi:10.3389/fnins.2019.00787

Tsvetanov, K. A., Henson, R. N., Tyler, L. K., Davis, S. W., Shafto, M. A., Taylor, J. R., . . . Rowe, J. B. (2015). The effect of ageing on fMRI: Correction for the confounding effects of vascular reactivity evaluated by joint fMRI and MEG in 335 adults. *Hum Brain Mapp, 36*(6), 2248-2269. doi:10.1002/hbm.22768

West, K. L., Zuppichini, M. D., Turner, M. P., Sivakolundu, D. K., Zhao, Y., Abdelkarim, D., . . . Rypma, B. (2019). BOLD hemodynamic response function changes significantly with healthy aging. *Neuroimage, 188*, 198-207. doi:10.1016/j.neuroimage.2018.12.012

Woolrich, M. W., Jbabdi, S., Patenaude, B., Chappell, M., Makni, S., Behrens, T., . . . Smith, S. M. (2009). Bayesian analysis of neuroimaging data in FSL. *Neuroimage, 45*(1 Suppl), S173-186. doi:10.1016/j.neuroimage.2008.10.055

Zhang, Y., Brady, M., & Smith, S. (2001). Segmentation of brain MR images through a hidden Markov random field model and the expectation-maximization algorithm. *IEEE Trans Med Imaging, 20*(1), 45-57. doi:10.1109/42.906424

Zhao, P., Alsop, D. C., Abduljalil, A., Selim, M., Lipsitz, L., Novak, P., . . . Novak, V. (2009). Vasoreactivity and peri-infarct hyperintensities in stroke. *Neurology, 72*(7), 643-649. doi:10.1212/01.wnl.0000342473.65373.80